INORGANIC CHEMISTRY
FRONTIERS

RESEARCH ARTICLE

View Article Online
View Journal | View Issue





Cite this: *Inorg. Chem. Front.*, 2019, **6**, 3196

# Electrochemical properties of chromium oxyfluoride $CrO_{2-x}F_x$ with $0 \le x \le 0.3$†

Kazuhiko Mukai, *[a] Takeshi Uyama [a] and Ikuya Yamada [b]

Received 24th June 2019,
Accepted 25th September 2019

DOI: 10.1039/c9qi00765b

rsc.li/frontiers-inorganic

To overcome the limitations of graphite as a negative electrode material for lithium-ion batteries (LIBs), transition metal oxyfluorides are under active development. In this study, chromium oxyfluorides $CrO_{2-x}F_x$ with $0 \le x \le 0.3$ were synthesized under a high-pressure/high-temperature (HP/HT) environment, and their electrochemical properties were examined in a nonaqueous lithium cell. The HP/HT-treated $CrO_2$ maintained a rutile structure and exhibited a rechargeable capacity ($Q_{recha}$) of over 400 mA h $g^{-1}$ at 298 K. The replacement of $O^{2-}$ ions with $F^-$ ions in $CrO_2$ was confirmed by linear changes in the tetragonal lattice parameters, weaker ferromagnetic interactions between $Cr^{4+}$ ions, and elemental mappings of $F^-$ ions. The $Q_{recha}$ values of the $x > 0$ samples at 298 K decreased to 150–300 mA h $g^{-1}$ because of low electric conductivity in $CrO_{2-x}F_x$. However, the $Q_{recha}$ values at 318 K increased to 600–700 mA h $g^{-1}$, and the cycle performance over 30 cycles was better than that of the HP/HT-treated $CrO_2$ sample with no $F^-$ substitution. Hence, $CrO_{2-x}F_x$ was found to be a promising negative electrode material for LIBs, although its cycle stability should be further improved.

## 1. Introduction

Transition metal (M) oxyfluorides with the general formula $M_aO_bF_c$ have recently received a great deal of attention as an electrode material for lithium-ion batteries (LIBs), although their synthesis and characterization date back to the 1950s.[1–3] The relevant electrochemical reaction is represented by

$$M_aO_bF_c + (2b + c)Li^+ + (2b + c)e^- \leftrightarrow aM + bLi_2O + cLiF, \quad (1)$$

where the theoretical capacity ($Q_{theo}$) is usually greater than that of graphite (=372 mA h $g^{-1}$),[4,5] which is currently used in conventional LIBs. This is because multiple electrons (*i.e.*, $2b + c$) are involved in the electrochemical reaction in $M_aO_bF_c$, in contrast to graphite, which involves a single electron.

Table 1 summarizes the crystal structures and electrochemical properties of the $M_aO_bF_c$ compounds reported thus far.[6–22] $NbO_2F$,[6,7] $TiF_2$[7,8,9,10] $TaO_2F$,[11] and $VO_2F$[12,13,14] have a regular or distorted $ReO_3$-type structure with a rechargeable capacity ($Q_{recha}$) of 200–400 mA h $g^{-1}$. Overall, their operating voltage as a function of $Q_{recha}$ is featureless, suggesting the same conversion reaction that is typical for their parent MO compounds.[23,24] On the other hand, $FeO_xF_{2-x}$ with a rutile structure[15–19] and $BiO_xF_{3-2x}$ with a tysonite-like structure[20,21] exhibited a flat operating voltage at ~2.4 and ~3.0 V, respectively, indicating a two-phase reaction. The $Q_{recha}$ values of $FeO_xF_{2-x}$[15–18] and $BiO_xF_{3-2x}$[20,21] are ~400 and ~200 mA h $g^{-1}$, respectively. An amorphous-like $MnOF_x$ phase[22] first showed a flat operating voltage at ~4.5 V owing to the release of oxygen from the lattice and then indicated a $Q_{recha}$ of ~225 mA h $g^{-1}$ at 0.0–3.0 V.

As understood by Table 1, all the $M_aO_bF_c$ compounds, except for $TiOF_2$, indicated higher operating voltages above 1.5 V or lower $Q_{recha}$ values below 300 mA h $g^{-1}$. Since the operating voltage and $Q_{recha}$ of graphite are ~0.2 V and ~330 mA h $g^{-1}$, respectively,[4,5] the energy density of LIBs would be decreased when employing the $M_aO_bF_c$ compounds as a negative electrode. Moreover, $M_aO_bF_c$ compounds are usually synthesized *via* solution routes using highly toxic, corrosive fluorine-containing acids or by ball milling a mixture of transition metal oxides and LiF.[6–22] These methods provide a bulky electrode material, lowering the volumetric energy density of LIBs. Hence, a denser $M_aO_bF_c$ compound with a $Q_{recha} > 330$ mA h $g^{-1}$ below ~1.0 V is required, to surpass the electrochemical properties of graphite and further increase the energy density of LIBs.[4,5]

[a]*Toyota Central Research & Development Laboratories, Inc., Yokomichi 41–1, Nagakute, Aichi, 480–1192, Japan. E-mail: e1089@mosk.tytlabs.co.jp; Fax: +81-561-63-6119; Tel: +81-561-71-7698*
[b]*Department of Materials Science, Graduate School of Engineering, Osaka Prefecture University, 1–2 Gakuen, Sakai, Osaka 599–8570, Japan*

†Electronic supplementary information (ESI) available: SEM images of the pristine $CrO_2$ sample, rietveld results of the pristine and HP/HT-treated $CrO_2$ samples, $V$ as a function of $x$ in $CrO_{2-x}F_x$, SEM images of the $x = 0.2$ and 0.3 samples, EPMA analyses of the $x = 0.20.2$ samples, cycle performance at 318 K of the HP/HT-treated $CrO_2$ sample, cycle performances at 318 K of the $x = 0.05$, 0.15, 0.2, and 0.3 samples, and XRD patterns of the $x = 0.2$ sample in the fully discharge state and after the cycle test at 318 K. See DOI: 10.1039/c9qi00765b

Table 1 Crystal structures and electrochemical properties of various transition metal oxyfluorides

| Compound | Crystal structure | Space group | Electrochemical properties | Synthesis method | Ref. |
|---|---|---|---|---|---|
| $NbO_2F$ | $ReO_3$-type (cubic) | $Pm\bar{3}m$ | 200 mA h $g^{-1}$ (0.005–3.0 V) | Solution route | 7 |
| $TiOF_2$ | (Distorted) $ReO_3$-type (cubic or rhombohedral) | $Pm\bar{3}m$ or $R\bar{3}c$ | 400 mA h $g^{-1}$ (0.005–3.0 V) | Solution route | 7 |
| $TaO_2F$ | $ReO_3$-type (cubic) | $Pm\bar{3}m$ | Unknown | Solution route | 11 |
| $VO_2F$ | Distorted $ReO_3$-type (rhombohedral) | $R\bar{3}c$ | 200 mA h $g^{-1}$ (2.0–4.5 V) | Ball-milling or HP | 14 |
| $FeO_xF_{2-x}$ | Rutile (tetragonal) | $P4_2/mnm$ | 450 mA h $g^{-1}$ (1.6–4.4 V) | Solid-state reaction | 15 |
| $BiO_xF_{3-2x}$ | Tysonite-like (orthorhombic) | $Pnma$ | 180 mA h $g^{-1}$ (2.0–4.5 V) | Solution route | 21 |
| $MnOF_x$ | Amorphous | | 225 mA h $g^{-1}$ (1.5–4.5 V) | Ball milling | 22 |
| $CrO_{2-x}F_x$ | Rutile (tetragonal) | $P4_2/mnm$ | 100–400 mA h $g^{-1}$ (0.02–3.0 V) | HP | This work |

In this study, we synthesized a series of $CrO_{2-x}F_x$ with $0 \leq x \leq 0.3$ using a high-pressure/high-temperature (HP/HT) method, and we examined their electrochemical properties, because chromium oxides, such as $Cr_2O_3$ [25–27] and $Cr_3O_8$,[25,28] have shown operating voltages below 1.0 V with ~500 mA h $g^{-1}$. Furthermore, $O^{2-}$ ions in $CrO_2$ have easily been substituted with $F^-$ ions under HP environments above 6 GPa,[2,3] providing dense $CrO_{2-x}F_x$ compounds. Here, $CrO_{2-x}F_x$, which has a rutile (tetragonal) structure with the $P4_2/mnm$ space group, exhibits ferromagnetic behavior above room temperature and is regarded as a promising spintronic material because of its nearly 100% spin polarization at the Fermi level.[3,29–32] To the best of our knowledge, the electrochemical properties of $CrO_{2-x}F_x$ including $CrF_2$ have never been reported, except for amorphous $CrO_{2-x}$ compounds with $0 \leq x \leq 0.5$.[33] Here, the $CrO_{2-x}F_x$ samples demonstrated a $Q_{recha}$ of 100–400 mA h $g^{-1}$ at 298 K and a $Q_{recha}$ of 600–700 mA h $g^{-1}$ at 318 K. The structural, magnetic, and electrochemical properties as a function of $x$ in $CrO_{2-x}F_x$ are discussed in detail.

## 2. Experimental

### 2.1. Sample preparation

Polycrystalline $CrO_2$ and $CrF_2$ powders provided by Kojundo Chemical Laboratory Co., Ltd (Japan) were mixed in various ratios using a mortar and a pestle in an argon-filled glove-box and then separately pressed into pellets with a diameter of 2.8 mm and a height of ~4 mm. The molar ratios of the different $CrO_2/CrF_2$ mixtures were 9 : 1, 8 : 2, 7 : 3, 6 : 4, or 4 : 6, forming a general chemical formula of $CrO_{2-x}F_x$ with $x$ = 0.05, 0.1, 0.15, 0.2, or 0.3. After being packed into a (Mg,Co)O pressure medium (Mino Ceramics Co., Ltd), the pellet was heated at 1273 K for 30 min under 12 GPa. The pellet consisting of only $CrO_2$ powder was also treated under the same conditions, and this sample is denoted by HP/HT-treated $CrO_2$. The HP/HT synthesis and experimental setup were described in detail elsewhere.[34–37]

### 2.2. Characterization

The particle morphologies of the synthesized samples were investigated using a scanning electron microscope (SEM; S-3600 N, Hitachi High-Technologies Co., Ltd). Approximately 1 mg of sample, which was attached onto the sample holder with carbon tape, was coated with electrically conducting Au particles (IB-3, Eiko Co., Ltd). To clarify the temperature at which the rutile structure converts to corundum, thermogravimetric/differential thermal analysis (TG/DTA) was conducted on pristine $CrO_2$ powder (Thermo plus EVO2, TG-DTA 8122, Rigaku Co., Ltd). Specifically, the sample was heated to 1273 K at 5 K $min^{-1}$ under air flowing at 100 mL $min^{-1}$.

X-ray diffraction (XRD) measurements were performed at the BL5S2 beamline of the Aichi Synchrotron radiation center. Each sample was inserted into a glass capillary tube with a diameter of 0.3 mm (WHM-Glas Müller Bmbh) to eliminate the effects of selective orientation. XRD patterns of the samples were recorded in the $2\theta$ range between 5 and 90° using Pilatus 100 K detectors. The X-ray wavelength was determined to be 0.799420(3) Å using a silicon standard (NIST 640d). Rietveld analyses were conducted using RIEATN-FP software,[38] and crystal structures were drawn using VESTA software.[39]

The magnetic susceptibilities ($\chi$) were examined using a superconducting quantum interference device (SQUID) magnetometer (MPMS, Quantum Design). $\chi$ was recorded in field-cooling (FC) mode with a magnetic field (H) of 10 kOe while the temperature decreased from 400 K to 5 K. Magnetization ($M$) *vs.* $H$ curves were also recorded at 5 K in the $H$ range between −55 and 55 kOe.

For only the $x$ = 0.2 sample, the distribution of Cr, O, and F atoms in the particles were examined using an electron probe microanalyzer (EPMA; JXA-8500F, JEOL Ltd) with an accelerating voltage of 15 kV. This is because as described later, the particle size of $CrO_{2-x}F_x$ drastically changed at $x \geq 0.2$. The sample was embedded in epoxy resin and then cut into a rectangle form using a cross-sectional polisher (SM-09010, JEOL Ltd) equipped with $Ar^+$ ions. The experimental procedure was similar to the one we used for our recent EPMA analysis of $LiCo_{0.64}Mn_{0.36}O_2$.[37]

### 2.3. Electrochemical measurements

Discharge and charge profiles were recorded using a non-aqueous lithium cell. The electrolyte was 1 M $LiPF_6$ dissolved in ethylene carbonate (EC)/diethylene carbonate (DEC) (EC/DEC = 1/1 by volume, Kishida Chemical Co., Ltd). A mixed electrode consisting of 70 wt% active material, 20 wt% conducting carbon (acetylene black, HS-100, Denka Co., Ltd), and 10 wt% polytetrafluoroethylene (PTFE) was used as the working electrode (diameter = 10 mm), while lithium metal

pressed onto a stainless steel plate (diameter = 19 mm) was used as the counter electrode. After being fabricating in the argon-filled glove-box, the lithium cells were operated at a current of 0.1 or 0.5 mA (≃0.1 or 0.5 mA $cm^{-2}$) between 0.02 and 3.0 V. The cells were tested at both 298 and 318 K. The lithium cells with the $x$ = 0 and 0.2 samples were cycled over 30 times at 298 and 318 K, and the rest of lithium cells were cycled over 5 cycles at 298 K. Above cycle tests were performed with a current of 0.1 mA. In addition, the lithium cells with $x$ = 0.05, 0.15, 0.2, and 0.3 were cycled over 50 cycles at 318 K with a current of 0.5 mA.

To clarify the reaction mechanism, *ex situ* XRD was performed at the BL5S2 beamline of the Aichi Synchrotron radiation center. The lithium cells with the $x$ = 0 and 0.2 samples were discharged down to 0.02 V, and then, in the argon-filled glove-box, the electrodes were removed. Each sample was packed into a glass capillary tube with a diameter of 0.7 mm (WHM-Glas Müller Bmbh), and XRD data were then recorded as for the initial samples. XRD patterns were also taken after the 30-cycle test ($x$ = 0 and 0.2). The X-ray wavelength was determined to be 0.799436(2) Å. The experimental conditions are described in further detail in the results and discussion section.

## 3. Results and discussion

### 3.1. HP/HT-treated $CrO_2$

Fig. 1a and b show SEM images of pristine $CrO_2$ and HP/HT-treated $CrO_2$ samples. Particles of the pristine $CrO_2$ exhibit a flake-like morphology with a lateral size of 5–50 μm and a thickness of ~2 μm. These flake-like particles consisted of numerous nanoscale particles, as shown in Fig. S1.† Particles of HP/HT-treated $CrO_2$ exhibit a non-uniform morphology with a smooth surface. The average size of the primary particles, which are aggregates of pristine $CrO_2$ particles, is approximately 20 μm.

Fig. 1c shows the TG/DTA curve of the pristine $CrO_2$ sample to clarify its thermal stability under ambient pressure. The weight of $CrO_2$ rapidly decreases starting at 766 K, and levels off to an almost constant value above 1073 K. The change in weight ($\Delta w$) above 1073 K was ~−10.0%, which was consistent with the calculated $\Delta w$ value (=−9.5%) based on the transformation of $CrO_2$ with a rutile structure into $Cr_2O_3$ with a corundum structure:

$$2CrO_2 \rightarrow Cr_2O_3 + 1/2O_2 \uparrow . \quad (2)$$

Despite the oxygen loss under ambient pressure, the HP environment stabilized the crystal structure of $CrO_2$. Fig. 1d and e show XRD patterns of the pristine $CrO_2$ and HP/HT-treated $CrO_2$ samples, respectively. The pristine $CrO_2$ sample contains only the rutile phase with lattice parameters of $a_t$ = 4.4224(1) Å and $c_t$ = 2.9160(1) Å. The corresponding Rietveld analysis results are shown in Fig. S2a.† The crystal structure of the HP/HT-treated $CrO_2$ sample is also assigned to the rutile structure, although a small amount of β-$CrO_2$ phase coexists in the sample (indicated by * in Fig. 1e). β-$CrO_2$, which considered a HP-form of $CrO_2$, adopts a distorted rutile structure with the *Pnnm* space group.[29] According to the Rietveld analysis results shown in Fig. S2b,† the weight fraction of the β-$CrO_2$ phase was estimated to be 6.5%. The lattice parameters of the major $CrO_2$ phase were determined to be $a_t$ = 4.4182(2) Å and $c_t$ = 2.9199(1) Å, which were comparable to those of the pristine $CrO_2$ sample.

Fig. 2a and b show the discharge and charge curves of the pristine $CrO_2$ and HP/HT-treated $CrO_2$ samples, respectively, operating at 298 K. Each discharge curve for the first cycle was

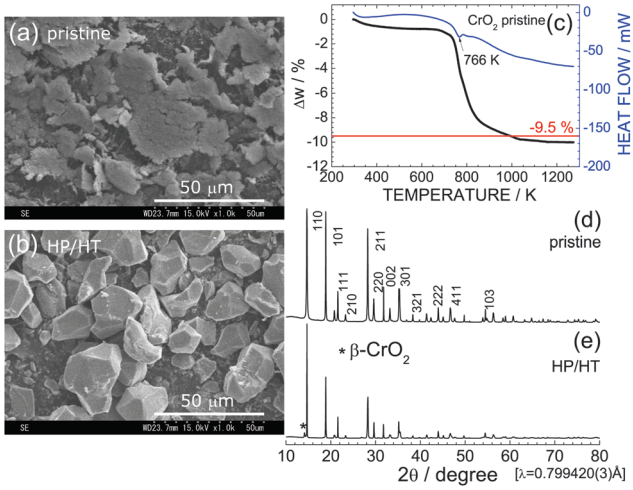


Fig. 1 SEM images of the (a) pristine $CrO_2$ and (b) HP/HT-treated $CrO_2$ samples. (c) The TG/DTA curve of the pristine $CrO_2$ sample. Synchrotron XRD patterns of the (d) pristine $CrO_2$ and (e) HP/HT-treated $CrO_2$ samples. The * symbol indicates the diffraction line from the β-$CrO_2$ phase.

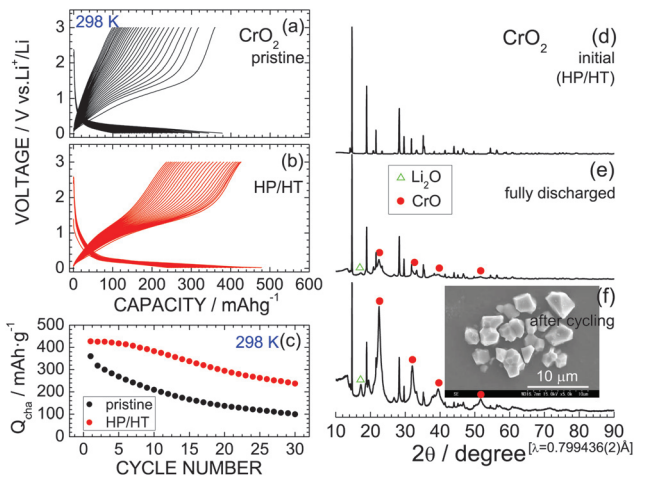


Fig. 2 Discharge and charge curves of the (a) pristine $CrO_2$ and (b) HP/HT-treated $CrO_2$ samples operated at 0.1 mA and 298 K. (c) Cycling performance of the two $CrO_2$ samples at 298 K. *Ex situ* XRD patterns of the HP/HT-treated $CrO_2$ samples: (d) initial state, (e) fully discharged state at 0.1 V, and (f) after cycling over 30 times. Inset: SEM image of the sample after cycling.

discarded to ignore the contributions of the decomposition reaction of the PTFE binder. The voltage of the pristine $CrO_2$ rapidly drops to ~0.4 V at the beginning of the discharge reaction and then maintains a constant value at ~0.2 V. The discharge capacity ($Q_{dis}$) reaches 377 mA h $g^{-1}$. The subsequent charge curve is quite different from the discharge curve, indicating a large voltage hysteresis of ~0.8 V. This is a typical characteristic of the conversion reaction, which occurs in various $M_aO_bF_c$ [6–22] and MO[23,24] compounds.

The discharge and charge curves of the HP/HT-treated $CrO_2$ sample were similar to those for the pristine $CrO_2$ sample; however, the values of $Q_{dis}$ and charge capacity ($Q_{cha}$) differed. Specifically, the maximum $Q_{cha}$ values for the pristine and HP/HT-treated $CrO_2$ samples were 360.1 and 427.0 mA h $g^{-1}$, respectively. Moreover, as shown in Fig. 2c, the cycling performance of the HP/HT-treated $CrO_2$ was superior to that of the pristine $CrO_2$. In addition, the pristine $CrO_2$ retained 27.6% of its capacity over 30 cycles, and the HP/HT-treated $CrO_2$ retained 55.6%. Note that this cycling test lasted for over one month because of the low current density of 0.1 mA $cm^{-2}$. This is a severe electrochemical test as the cells were exposed to low voltages below 0.5 V for a long time. The cycle test at such low current densities has also been applied to the preliminary evaluation of $LiNi_{1/2}Mn_{1/2}O_2$ [40] and $LiCo_{1/3}Ni_{1/3}Mn_{1/3}O_2$.[41]

The complete conversion reaction is represented by

$$CrO_2 + 4Li^+ + 4e^- \leftrightarrow Cr + 2Li_2O, \quad (3)$$

where $Q_{theo}$ is calculated to be 1276.3 mA h $g^{-1}$. Multiple electrons also involve in the electrochemical reactions of other oxides[42] and sulfur compounds.[43,44] The observed $Q_{recha}$ of the HP/HT-treated $CrO_2$ was limited to approximately one-third of $Q_{theo}$. To clarify the origins of such a significant decrease in capacity, *ex situ* XRD measurements were conducted in the fully discharged state. Fig. 2d–f show the XRD patterns in the initial state, fully discharged state down to 0.1 V, and after cycling over 30 times, respectively. In the fully discharged state, broad diffraction lines appear at around $2\theta$ = 22.4, 32.2, 39.4, and 51.7°, which are each assigned to a diffraction line of CrO with $Fm\bar{3}m$ space group (PDF-4+01-073-9520).[45] The cubic lattice parameter ($a_c$) of the CrO phase was calculated to be ~4.10 Å. The diffraction line at $2\theta$ = 17.3° ($d \simeq 2.66$ Å) is indexed to the 111 diffraction line of $Li_2O$ (PDF-4+04-008-3420).[45] Continuous cycling strengthens the intensities of the CrO and $Li_2O$ phase peaks, thus demonstrating that the initial $CrO_2$ phase transforms into an amorphous-like phase with continued cycling. The actual electrochemical reaction of $CrO_2$ is thus represented by

$$CrO_2 + 2Li^+ + 2e^- \leftrightarrow CrO + Li_2O, \quad (4)$$

where $Q_{theo}$ is calculated to be 638.2 mA h $g^{-1}$. The formation of the CrO phase instead of the Cr metal is caused by the low operating voltage (~0.2 V) during the discharge reaction; $RuO_2$, for instance, exhibited an operating voltage of ~0.8 V when the Ru metal was formed in the particles.[23]

### 3.2. $CrO_{2-x}F_x$

Fig. 3a–e show the XRD patterns of the $CrO_{2-x}F_x$ samples with $x$ = 0.05, 0.1, 0.15, 0.2, and 0.3. All the XRD patterns were assigned to the rutile structure, similar to the $x$ = 0 samples. The $Cr_2O_3$ impurity was observed in the $x$ = 0.2 and 0.3 samples. The $a_t$ and $c_t$ values, which were determined *via* Rietveld analyses, are shown in Fig. 3f and g, respectively, which also show reported $a_t$ and $c_t$ values.[3] The lattice parameters $a_t$ and $c_t$ in this study increase almost monotonically with $x$, indicating that as expected, $O^{2-}$ ions are substituted by $F^-$ ions. The lattice volume ($V$) obtained by $a_t^2 \times c_t$ are shown in Fig. S3.† However, these lattice parameters were slightly lower than those of the reported values,[3] particularly at $x \geq 0.2$. Recently, anion ordering between $O^{2-}$ and $F^-$ ions appeared in the electron diffraction patterns of $CrO_{2-x}F_x$ with $x$ = 0.1, 0.12, and 0.14.[31] In contrast, because the X-ray scattering factors of $O^{2-}$ and $F^-$ ions are similar to each other in this study, such anion ordering is not observed in the XRD measurements.

The SEM images in the inset of Fig. 3a–e clearly show that substituting $F^-$ for $O^{2-}$ altered the particle sizes of $CrO_{2-x}F_x$. The average size of primary particles is approximately 10 μm for the $x \leq 0.15$ samples, whereas it is less than 3 μm for the $x$ = 0.2 and 0.3 samples. The drastic change in the particle size was also observed on the HP/HT studies on $Li[Li_{1/3}Ti_{5/3}]O_4$.[34] Enlarged SEM images for the $x$ = 0.2 and 0.3 samples are shown in Fig. S4.†

Since $CrO_2$ exhibited ferromagnetic behavior with a Curie temperature ($T_C$) of ~390 K,[3,29–32] the effects of substituting $F^-$ for $O^{2-}$ ions were investigated from the aspect of magnetism. Fig. 4a and b show the temperature dependence of $\chi$ and $\chi^{-1}$ measured in the FC mode with $H$ = 10 kOe. As the temperature decreases from 400 K, $\chi$ of the pristine $CrO_2$ sample increases

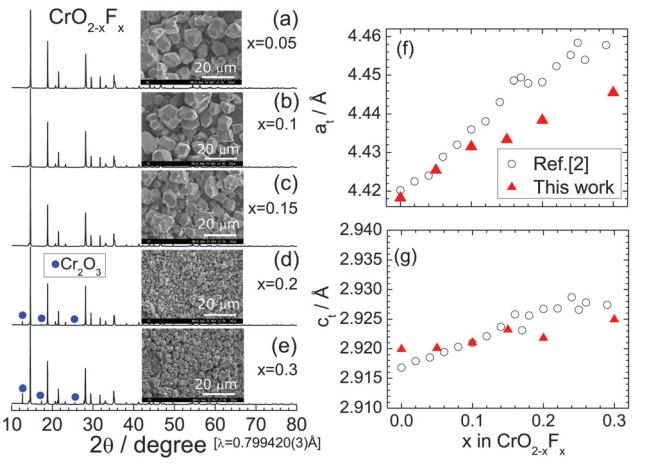


**Fig. 3** Synchrotron XRD patterns of the $CrO_{2-x}F_x$ samples with (a) $x$ = 0.05, (b) $x$ = 0.1, (c) $x$ = 0.15, (d) $x$ = 0.2, and (e) $x$ = 0.3. An SEM image of each sample is shown in the inset. Diffraction lines from the $Cr_2O_3$ phase are indicated by circles. Lattice parameters (f) $a_t$ and (g) $c_t$ as a function of $x$ in $CrO_{2-x}F_x$, including the $a_t$ and $c_t$ values reported in ref. 2.

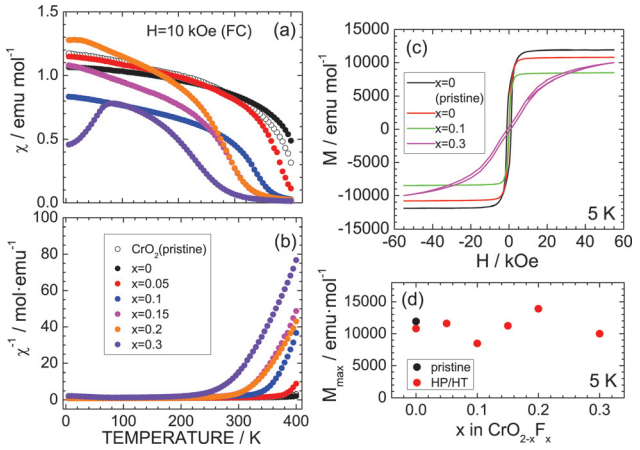


**Fig. 4** (a) $\chi$ and (b) $\chi^{-1}$ of the $CrO_{2-x}F_x$ samples with $x$ = 0, 0.05, 0.1, 0.15, 0.2, and 0.3. (c) $M$–$H$ curve of the $CrO_{2-x}F_x$ samples with $x$ = 0, 0.1, and 0.3 at 5 K. The two $x$ = 0 samples in (a)–(c) are the pristine $CrO_2$ and HP/HT-treated $CrO_2$ samples. (d) $M$ at $H$ = 55 kOe, *i.e.*, $M_{max}$, as a function of $x$ in $CrO_{2-x}F_x$.

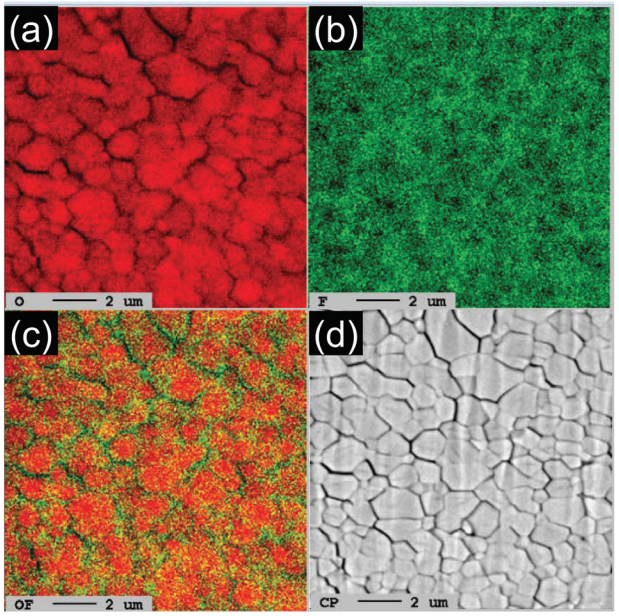


**Fig. 5** EPMA results from the $x$ = 0.2 sample: mappings of (a) O and (b) F and (c) overlapping mapping of O and F atoms. (d) Corresponding SEM image. Scale bars: 2 μm scale.

from ~0.5 emu $mol^{-1}$ to ~0.9 emu $mol^{-1}$ and then maintains an almost constant value (~1.0 emu $mol^{-1}$) below 200 K. Similar behavior is also observed in the $\chi$ (or $\chi^{-1}$) *vs.* temperature curves of the $x$ = 0, 0.05, 0.1, 0.15, and 0.2 samples. However, the $x$ = 0.3 sample indicates a slightly different trend, especially below 100 K, wherein $\chi$ rapidly drops to ~0.45 emu $mol^{-1}$ at 5 K. This decrease in $\chi$ is attributed to partial antiferromagnetic $Cr^{4+}$–$Cr^{3+}$ interactions produced by the $F^-$ ion substitution.[29,30] Antiferromagnetic interactions also appear in the $M$–$H$ curves at 5 K (Fig. 3c). The pristine $CrO_2$ sample shows soft ferromagnetic behavior with a maximum (saturation) $M$ ($M_{max}$) of ~11 900 emu $mol^{-1}$. This $M_{max}$ value corresponds to ~2.1$\mu_B$, which is consistent with the spin-only calculated magnetic moment (=2$\mu_B$) assuming that $Cr^{4+}$ ions are in the $t_{2g}^2$ (S = 1) state. Substituting $F^-$ ions for $O^{2-}$ ions decreases the $M_{max}$ value, except for the $x$ = 0.2 sample (Fig. 4d). Moreover, the $M$–$H$ curve for $x$ = 0.3 is a competitive consequence of ferromagnetic interactions between $Cr^{4+}$ ions and antiferromagnetic interactions between $Cr^{4+}$ and $Cr^{3+}$ ions.

To clarify the distributions of O and F atoms in $CrO_{2-x}F_x$ particles, Fig. 5 shows the EPMA mapping results from the $x$ = 0.2 sample for O and F atoms. O and F atoms are distributed throughout the entire particles, but F is slightly localized near the surface of the particles. This means that the $F^-$ ions are inhomogeneously distributed inside the particles, although the lattice parameters $a_t$ and $c_t$ increased almost linearly with $x$. Cr, O, and F atoms are mapped at the 1 μm scale in Fig. S5.†

Fig. 6a–e show the discharge and charge curves of the $x$ = 0.05, $x$ = 0.1, $x$ = 0.15, $x$ = 0.2, and $x$ = 0.3 samples operated at 298 K. For comparison, the discharge and charge curves of $CrF_2$ are also shown in Fig. 6f. For the $x$ = 0.05 sample, the $Q_{dis}$ and $Q_{cha}$ values during the initial cycle are 399.0 and 364.4 mA h $g^{-1}$, respectively, which are slightly lower than

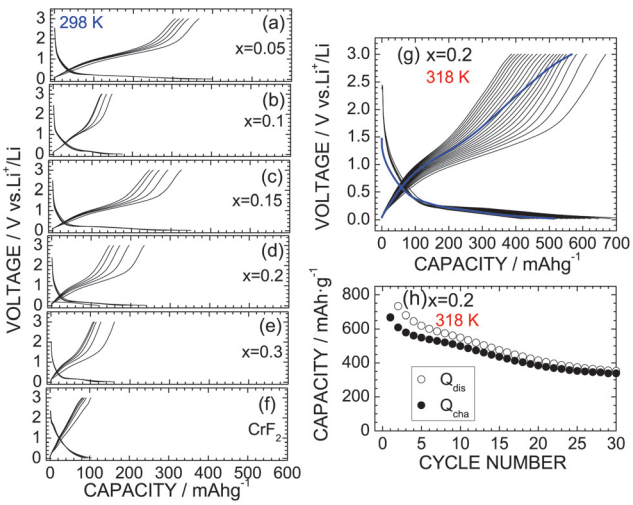


**Fig. 6** Discharge and charge curves of the $CrO_{2-x}F_x$ samples with (a) $x$ = 0.05, (b) $x$ = 0.1, (c) $x$ = 0.15, (d) $x$ = 0.2, (e) $x$ = 0.3, and (f) $CrF_2$ operated at 298 K. (g) Discharge and charge curves of the $x$ = 0.2 sample operated at 318 K. (h) Cycling performance of the $x$ = 0.2 sample at 318 K. The blue lines in (c) indicate the discharge and charge curves at a low current density of ~0.03 mA $cm^{-2}$ after the cycle test.

those for the HP/HT-treated $CrO_2$ ($x$ = 0) sample. However, as $x$ increases from $x$ = 0.05, both $Q_{dis}$ and $Q_{cha}$ decrease to 150–300 mA h $g^{-1}$ due to a low electrical conductivity, which has also been observed with other oxyfluoride materials.[6–22] Since the operating voltage of the discharge reaction was close to the discharge cut-off voltage ( = 0.02 V), the discharge reaction of the $CrO_{2-x}F_x$ compounds finished before storing a

large amount of Li ions. Note that $CrF_2$ exhibits a $Q_{recha}$ of ~100 mA h $g^{-1}$ and a capacitor-like voltage profile.

The lithium cells with the $x = 0$ and 0.2 samples were also cycled at 318 K to clarify the cycle stability at high temperatures. Fig. 6g shows the discharge and charge curves of the $x = 0.2$ sample at 318 K with a current of 0.1 mA, and Fig. 6h shows the corresponding cycle performance over 30 cycles. The $Q_{dis}$ and $Q_{cha}$ values during the initial cycle are 773.1 and 667.3 mA h $g^{-1}$, respectively, which are approximately three times larger than those at 298 K. Although the $Q_{cha}$ value decreases with cycling, it remains at 338.8 mA h $g^{-1}$ after 30 cycles, thus providing a capacity retention of 50.8%. Note that this capacity retention is superior to that of the HP/HT-treated $CrO_2$ at 318 K, wherein 40.0% of the capacity was retained (see Fig. S6†). Furthermore, as shown in Fig. S7,† the capacity fading at 318 K was suppressed by the substitution of F ions, especially at the latter of 50 cycles. According to the *ex situ* XRD measurements, the CrO phase with $a_c = 4.09$ Å was produced in the fully discharged state (Fig. S8b†). Furthermore, the diffraction line at $2\theta \simeq 17.3°$ was hardly observed, indicating that the substitution of $F^-$ ions suppresses the formation of the $Li_2O$ phase. This is probably due to the strong ionic interaction between the $Cr^{4+}$ and $F^-$ ions. Since the initial rutile structure of $CrO_{2-x}F_x$ transformed into an amorphous phase after the cycling test (Fig. S8c†), the discharge and charge reactions of $CrO_{2-x}F_x$ proceed between the CrO and amorphous phases, unlike the electrochemical reaction described in eqn (1).

Finally, we discuss the significance of the $CrO_{2-x}F_x$ materials as a negative electrode for LIBs. The operating voltage in the discharge reaction was close to 0.2 V, which is the lowest operating voltage observed for oxyfluorides (Table 1) and is similar to that of the graphite. Furthermore, the theoretical density of $CrO_{2-x}F_x$ according to the XRD data is ~4.89 g $cm^{-3}$, which is two times larger than that of the graphite (≃2.2 g $cm^{-3}$). Since LIBs are the device that functions in a limited space, $CrO_{2-x}F_x$ is a promising negative electrode material for LIBs in terms of volumetric energy density. However, even with the $x = 0.2$ sample, the cycle stability of $CrO_{2-x}F_x$ is not sufficient for practical LIB applications. According to the electrochemical measurements after the cycle test at 318 K, both $Q_{dis}$ and $Q_{cha}$ values recovered to ~87% of their initial values at the low current density of ~0.03 mA $cm^{-2}$ (Fig. 6g). Hence, the capacity fading in $CrO_{2-x}F_x$ is caused not by a destruction of the core material but by a failure of contact between the active material and the conducting carbon. Further optimizing the electrode mixture and the type of conducting carbon and/or binders could improve the cycle performance of $CrO_{2-x}F_x$.

## 4. Conclusion

The HP/HT-treated $CrO_2$ maintained the rutile structure even after heating at 1273 K and exhibited a $Q_{recha}$ of 400 mA h $g^{-1}$ at 298 K. The operating voltage of the discharge reaction was close to 0.2 V, which is the lowest reported operating voltage among oxyfluoride materials such as $FeO_xF_{2-x}$ and $BiO_xF_{3-2x}$. $F^-$ ions successfully replaced the $O^{2-}$ ions in $CrO_2$ under the HP/HT environment, providing a linear increase in the lattice parameters $a_t$ and $c_t$ and weakening the ferromagnetic interaction between $Cr^{4+}$ ions. The $Q_{recha}$ values of the $x > 0$ samples decreased to 150–300 mA h $g^{-1}$ at 298 K but increased to more than 600 mA h $g^{-1}$ at 318 K. The cycle performance of $x = 0.2$ at 318 K was superior to that of the HP/HT-treated $CrO_2$ sample, suggesting that the substitution of $F^-$ ions stabilized the crystal lattice during the discharge and charge reactions at high temperatures. The electrochemical properties of $CrO_{2-x}F_x$ are promising as an alternative of graphite, the most popular negative electrode material in LIBs. Furthermore, the present results provide a new direction for synthesizing (lithium) oxyfluoride materials with a large volumetric energy density.

## Conflicts of interest

There are no conflicts to declare.

## Acknowledgements

The authors wish to thank Dr Takao Inoue of TCRDL for help with the HP/HT syntheses and Mr Yusuke Yagi of TCRDL for the EPMA analysis. The synchrotron XRD patterns were measured at the BL5S2 beamline of the Aichi Synchrotron Radiation Center, Aichi Science & Technology Foundation, Japan (Proposal No. 201803038 and 201901008).

## References

1 K. Vorres and J. Donohue, *Acta Crystallogr.*, 1955, **8**, 25.
2 B. L. Chamberland, A. W. Sleight and W. H. Cloud, *J. Solid State Chem.*, 1970, **2**, 49.
3 B. L. Chamberland, C. G. Frederick and J. L. Gillson, *J. Solid State Chem.*, 1973, **6**, 561.
4 T. Ohzuku, Y. Iwakoshi and K. Sawai, *J. Electrochem. Soc.*, 1993, **140**, 2490.
5 K. Mukai, T. Inoue and M. Hasegawa, *J. Power Sources*, 2017, **366**, 185.
6 C. Bohnke, J. L. Fourquet, N. Randrianantoandro, T. Brousse and O. Crosnier, *J. Solid State Electrochem.*, 2001, **5**, 1.
7 M. V. Reddy, S. Madhavi, G. V. Subba Rao and B. V. R. Chowdari, *J. Power Sources*, 2006, **162**, 1312.
8 B. Li, D. Wang, Y. Wang, B. Zhu, Z. Gao, Q. Hao, Y. Wang and K. Tang, *Electrochim. Acta*, 2015, **180**, 894.
9 C. Evangelisti, M. Hayatifar, F. Marchetti, M. Marelli, G. Pampaloni and F. Piccinelli, *Inorg. Chem.*, 2016, **55**, 1816.
10 N. Luovain, Z. Karkar, M. El-Ghozzi, P. Bonnet, K. Guérin and P. Willmann, *J. Mater. Chem. A*, 2014, **2**, 15308.

11 J. Dabachi, M. Body, C. Galven, F. Boucher and C. Legein, *Inorg. Chem.*, 2017, **56**, 5219.
12 J. C. Pérez-Flores, R. Villamor, D. Ávila-Brande, J. M. Gallardo Amores, E. Morán, A. Kuhn, F. García-Alvarado, M. Bervas, B. Yakshinskiy, L. C. Klein and G. G. Amatucci, *J. Mater. Chem. A*, 2015, **3**, 20508.
13 R. Chen, E. Maawad, M. Knapp, S. Ren, P. Beran, R. Witter and R. Hempelmann, *RSC Adv.*, 2016, **6**, 65112.
14 M. A. Cambaz, B. P. Vinayan, O. Clemens, A. R. Munnangi, V. S. K. Chakravadhanula, C. Kübel and M. Fichtner, *Inorg. Chem.*, 2016, **55**, 3789.
15 N. Pereira, F. Badway, M. Wartelsky, S. Gunn and G. G. Amatucci, *J. Electrochem. Soc.*, 2009, **156**, A407.
16 I. D. Gocheva, I. Tanaka, T. Doi, S. Okada and J. Yamaki, *Electrochem. Commun.*, 2009, **11**, 1583.
17 L. Li, F. Meng and S. Jin, *Nano Lett.*, 2012, **12**, 6030.
18 S.-W. Kim, N. Pereira, N. A. Chernova, F. Omenya, P. Gao, M. S. Whittingham, G. G. Amatucci, D. Su and F. Wang, *ACS Nano*, 2015, **10**, 10076.
19 M. Burbano, M. Duttine, B. J. Morgan, O. J. Borkiewicz, K. W. Chapman, A. Wattiaux, A. Demourgues, H. Groult, M. Salanne and D. Dambournet, *J. Phys. Chem. Lett.*, 2019, **10**, 107.
20 M. Bervas, B. Yakshinskiy, L. C. Klein and G. G. Amatucci, *J. Am. Ceram. Soc.*, 2006, **89**, 645.
21 M. Bervas, L. C. Klein and G. G. Amatucci, *J. Electrochem. Soc.*, 2006, **153**, A159.
22 L. Zhang, D. Dambournet, A. Iadecola, D. Batuk, O. J. Borkiewicz, K. M. Wiaderek, E. Sakager, M. Shao, G. Chen and J.-M. Tarascon, *Chem. Mater.*, 2018, **30**, 5362.
23 Y.-Y. Hu, Z. Liu, K.-W. Nam, O. J. Borkiewicz, J. Chung, X. Hua, M. T. Dunstan, X. Yu, K. M. Wiaderek, L.-S. Du, K. W. Chapman, P. J. Chupas, X.-Q. Yang and C. P. Grey, *Nat. Mater.*, 2013, **12**, 1130.
24 H.-F. Wang, C. Tang, B.-Q. Li and Q. Zhang, *Inorg. Chem. Front.*, 2018, **5**, 521.
25 Y. Takeda, R. Kanno, Y. Tsuji and O. Yamamoto, *J. Power Sources*, 1983, **9**, 325.
26 J. Hu, H. Li and X. Huang, *Electrochem. Solid-State Lett.*, 2005, **8**, A66.
27 L.-Y. Jiang, S. Xin, X.-L. Wu, H. Li, Y.-G. Guo and L.-J. Wan, *J. Mater. Chem.*, 2010, **20**, 7565.
28 R. Koksbang and P. Norby, *Electrochim. Acta*, 1991, **36**, 127.
29 B. R. Maddox, C. S. Yoo, D. Kasinathan, W. E. Pickett and R. T. Scalettar, *Phys. Rev. B: Condens. Matter Mater. Phys.*, 2006, **73**, 144111.
30 W. Ren, B. Li, W. Liang, C. Jin and Z. Zhang, *J. Alloys Compd.*, 2014, **596**, 69.
31 B. Li, Y. Chen, H. Wang, W. Liang, G. Liu, W. Ren, C. Li, Z. Liu, G. Rao, C. Jin and Z. Zhang, *Chem. Commun.*, 2014, **50**, 799.
32 S. Huang, X. Wu, J. Niu and S. Qin, *RSC Adv.*, 2018, **8**, 24561.
33 J. Kim and A. Manthiram, *J. Electrochem. Soc.*, 1997, **144**, 3077.
34 K. Mukai and I. Yamada, *Inorg. Chem. Front.*, 2018, **5**, 1941.
35 T. Uyama, K. Mukai and I. Yamada, *RSC Adv.*, 2018, **8**, 26325.
36 K. Mukai, T. Uyama and I. Yamada, *ACS Omega*, 2019, **4**, 6459.
37 T. Uyama, K. Mukai and I. Yamada, *Inorg. Chem.*, 2019, **58**, 6684.
38 F. Izumi and K. Momma, *Solid State Phenom.*, 2007, **130**, 15.
39 K. Momma and F. Izumi, *J. Appl. Crystallogr.*, 2011, **44**, 1272.
40 T. Ohzuku and Y. Makimura, *Chem. Lett.*, 2001, **7**, 744.
41 N. Yabuuchi and T. Ohzuku, *J. Power Sources*, 2003, **199–121**, 171.
42 S. Deng, Y. Zhang, D. Xie, L. Yang, G. Wang, X. Zheng, J. Zhu, X. Wang, Y. Yu, G. Pan, X. Xia and J. Tu, *Nano Energy*, 2019, **58**, 355.
43 B. Liu, R. Fang, D. Xie, W. Zhang, H. Huang, Y. Xia, X. Wang, X. Xia and J. Tu, *Energy Environ. Mater.*, 2018, **1**, 196.
44 S. Liu, X. Xia, S. Deng, D. Xie, Z. Yao, L. Zhang, S. Zhang, X. Wang and J. Tu, *Adv. Mater.*, 2019, **31**, 1806470.
45 PDF-4+: Powder Diffraction File; International Centre for Diffraction Data: Newtown Square, PA, 2004.

 